

A meso-scale solidification simulation of fusion welding in Aluminum-Magnesium-Silicon alloys

H.R. Zareie Rajani^{a, 1}, A.B. Phillion^{a, 2}

^a Okanagan School of Engineering, University of British Columbia, Kelowna, BC, Canada

¹ hamid.zareie.rajani@ubc.ca, ² andre.phillion@ubc.ca

Abstract

A 3D granular model has been developed to simulate solidification during fusion welding of Al alloys. The model simulates the gradual development of the weld mushy zone composed of both continuous liquid films and solidifying grains by coupling thermal fields based on the Rosenthal equation, a modified Voronoi tessellation to provide grain structure at the meso-scale, and the evolution in fraction solid within a grain based on the Scheil equation. The shape and geometry of the columnar and equiaxed grains within the weld pool has been characterized from experiments and therefore the model can be used to link the solidification behaviour of individual grains to the macroscopic properties of the weld. The gradual formation of micro liquid channels lying along the grain boundaries within the mushy zone is investigated and the role of welding parameters including amperage and welding speed on transitions in the semi solid microstructure is explored. The study reveals that the ability of the micro liquid channels to feed molten metal into the solidifying areas is not uniform through the weld, and is strongly affected by grain size since smaller grains hinder the feeding ability of the mushy zone.

Keywords: Solidification; Welding; Modelling; Microstructure; Meso-scale.

1. Introduction

During fusion welding of aluminum alloys, restraining forces may arise due to component geometry, clamping configuration and thermal contraction, and lead to tensile stresses along the fusion line. If not properly controlled, the result of these stresses is a solidification defect known as hot cracking [1] that significantly lowers weldability. A hot crack forms and grows behind the weld pool, within the two-phase mushy zone, rupturing liquid films that are present at grain boundaries [2]. In addition to tensile stresses, the formation of a hot crack in welding is strongly linked to the grain morphology. The initiated micro-cracks within the mushy zone will only survive if the microstructure configuration does not allow for liquid feeding to heal the hot crack [3]. Knowledge of the transient microstructure of the semisolid weld pool not only gives insights into hot crack survival, but also contributes to an understanding of other transient phenomena within the mushy zone, including molten metal flow characteristics and defect formation.

The high temperature condition in welding and the very short lifetime of the semisolid weld pool restrict the application of experimental methods for investigating the transient microstructure of the weld. Instead, numerical techniques are most often used [2]. In the past few years, four major complementary techniques have been developed to model solidification at the scale of the microstructure: front tracking, phase-field, cellular automaton (CA), and granular or discrete-based methods. The first two techniques work rather well to reproduce most phenomena associated with microstructure evolution, but as the mesh size must remain small, the simulation is limited to modelling only a few grains due to computational cost. In welding, these techniques have been implemented to study the solidification morphology of grains [4], and also the columnar-to-

equiaxed transition phenomenon [5]. In contrast, the cellular automaton (CA) method has had much success in modelling solidification structure. For welding, this technique has been used to model the competitive growth process between columnar and equiaxed grains, and also to predict the weld microstructure in two dimensions [6]. The CA method has also recently been applied to model hot cracking in welding [7], showing that the susceptible sites to hot cracking are normally located along columnar grain boundaries. However, this technique does not lend itself to investigating microstructure transitions since the solid and liquid phases are not explicitly defined. Knowledge of such transitions is a key factor for reducing hot cracking susceptibility.

The so-called granular model of solidification [8-13] is a recently developed numerical technique in which an assembly of discrete elements is used to simulate equiaxed-globular solidification. The main advantage of this technique is its use of discrete elements, which allows for the simulation of large and non-isothermal mushy zones, as well as inclusion of stochastic effects and solid/liquid interactions [3, 11, and 12]. In this model, grains are approximated by polyhedrons based on the Voronoi diagram of a random set of nuclei, resulting in irregular grain arrangements. Solidification is then carried out [12] by advancing the grain edges towards the border along a linear segment connecting the nuclei with a Voronoi vertex. Vernède et al. [3, 8, 11] first developed a comprehensive model of this type based on an original idea of Mathier et al. [13] to simulate in two dimensions the solidification sequence and grain percolation of an Al-Cu binary alloy. The authors were able to link the behaviour of the grain network to the macroscopic properties of the semisolid material. Later, Phillion et al. [12] extended this approach to a three-dimensional domain (3D), and showed that the extension to 3D allows for concurrent continuity of both the liquid and solid phases. Such a concurrent continuity is a key factor for semisolid defect formation. Granular-

type models have also been used by Sistaninia et al. [9, and 10], Phillion et al. [14], and Zaragoci et al. [15] to investigate semisolid deformation and crystal rearrangement.

Although the previous granular models of solidification have provided much insight into the stochastic microstructure variability, structure transitions from a continuous liquid to coherent solid, and also grain percolation, the basic assumptions of equiaxed-globular microstructure and uniform cooling rates do not apply in complex casting processes such as die-casting and welding where the solidification kinetics are highly complex. In the case of welding, the fast variable cooling rates containing strong non-linear thermal gradients must be taken into account, along with spatial variations in grain morphology that depend on process parameters. In this study, a meso-scale model is presented that simulates in three dimensions the transient two-phase microstructure of the semisolid weld pool during tungsten inert gas (TIG) welding of an industrial aluminum-magnesium-silicon alloy, AA6061. The microstructure is modelled based on a granular approach, while reproducing a weld domain that is large enough to relate the microstructure and stochastic effects to macroscopic properties. In the first part of this work, a meso-scale model of solidification during welding is developed. Results from welding experiments that are used as input to link the final as-solidified microstructure of the weld pool with processing conditions are also given. Then, meso-scale observations of the solidification sequence during welding are analyzed. Finally, mushy zone morphology maps calculated from the model as a function of process parameters are discussed.

2. Model description

2.1. Simulation domain

2.1.1. Size and Geometry of the RVE

The simulation domain for investigating microstructure evolution during fusion welding of aluminum alloys is illustrated in Fig. 1. Due to symmetry, only one-half of the weld is included. This 3D representative volume element (RVE) can be described through both its macroscopic and microscopic characteristics.

At the macro-scale, the simulation domain must encompass the entire cross-section of the weld zone in order to be considered an RVE, and therefore, its size is determined from the depth of penetration and width of the weld assuming a parabolic cross-sectional fusion zone. A small amount of base metal is also included in order to create a cuboid domain. The white dashed cube in Fig. 1 indicates the shape and position of the RVE with respect to time and the position of the weld torch. The origin of the RVE is denoted by O , the penetration depth and width of the weld respectively lie along the X and Y directions, and the Z direction follows the line of welding. The RVE covers one-half of the weld, and at the beginning of the analysis (welding time equals zero), the weld center, identified by a small white circle in Fig. 1, is assumed to be located at an arbitrary position of $X=1$, $Y=1$, and $Z=0$. With time, the weld torch advances, moving through then out of the RVE, creating transient conditions for solidification. Note that the total weld length simulated along the Z -direction is equivalent to one-third of the mushy zone.

At the scale of the microstructure, the simulation domain must contain substructure consisting of base metal equiaxed grains, columnar fusion zone grains, and then equiaxed fusion zone grains near the weld centre in order to be considered an RVE [16]. Such a substructure enables direct simulation of the evolution of the weld microstructure during solidification. This substructure is created within the simulation domain by further discretizing the RVE using an unstructured meshing technique; the methodology for discretization will be presented in Section 2.1.3.

2.1.2. Creating a Welding Parameters-Dependant RVE

As outlined above, a meso-scale solidification simulation of fusion welding requires as input the weld depth of penetration, the weld width, and the length of the columnar zone. Further, as the weld's macrostructure and microstructure are strongly linked to the applied welding conditions [16, 17], these characteristics of the simulation domain must vary as a function of welding parameters. Otherwise the model cannot simulate the role of welding procedure in the formation of the semisolid weld and defects.

In order to create a map linking the simulation input parameters to welding parameters, specifically welding speed and welding amperage, a series of 28 bead-on-plate weld experiments were conducted and then analyzed via optical and scanning-electron microscopy. The resulting relation defines the variation of the RVE as a function of welding procedure. Fig. 2a and b illustrate the applied measurement methodology, while Fig. 3a and b provides process maps for the weld depth of penetration and weld width. Electron Backscattered Diffraction (EBSD) imaging was then used to detect the location of the columnar zone within the fusion weld pool and to calculate an average columnar grain length. The process map for this characteristic is shown in Fig. 3c. Note that the values for columnar grain length have been normalized with respect to the depth of penetration since smaller welds normally have smaller absolute values for columnar grains and vice versa.

The obtained process maps can be utilized as input data since they link the macroscopic and microscopic characteristics of an AA 6061 weld to welding parameters, and therefore enable the simulation domain to vary based on an assumed welding procedure. As can be seen in Fig. 3, high welding currents leading to high welding powers, and slow welding speeds will yield RVEs with larger welds and a microstructure in which the columnar zone is shrunk. On the other hand,

lowering the welding power and increasing the welding speed will lead to RVEs with smaller welds and longer columnar grains.

2.1.3. Mesh

The unstructured mesh representing the final as-solidified grain structure within the RVE is generated using a 3D Voronoi tessellation of the simulation domain whereby grains are approximated by polyhedrons based on the Voronoi diagram of a random set of nuclei. The Voronoi tessellation is a technique of dividing spatial domains into numbers of subzones. A set of points (called seeds) is first specified within the domain and for each seed there will be a corresponding zone consisting of all points closer to that seed than to any other. The developed subzones are called Voronoi cells. It has previously been shown that the final structure for grain-refined alloys with equiaxed-globular microstructure is close to a Voronoi tessellation of random nucleation centres [8-10]. However, welding microstructure is considerably more complex, and thus the Voronoi tessellation of a random set of nuclei requires some modification to be applicable in this situation. At the meso-scale, the RVE consists of three separate regions: base metal, columnar zone, and equiaxed zone at the center of the weld. In order to extend the basic Voronoi tessellation to create such a complex microstructure, a purpose-written C++ code was developed that divides the domain into three separate regions, creates individual Voronoi diagrams within each region, and then combines all the nodes and elements together to create a single continuous mesh. First, the code uses the data from the welding experiments shown in Fig. 3 to determine the size, position and shape of each region for a given set of welding parameters assuming a parabolic interface. Second, grain nuclei are placed within each region and then a Voronoi tessellation for each region is computed. For base metal and equiaxed zone regions, grain nuclei are placed randomly corresponding to a given grain density. For the columnar zone region, grain nuclei are

placed along a centerline so that the resulting grains are columnar in shape. It is assumed that the epitaxial growth governs the formation of columnar grains [16] and thus the average diameter of the columnar grains is close to the size of the equiaxed grains within the base metal, while the length of the columnar grains is taken from the experimental data. Third, once all the Voronoi tessellations of the three regions are created, coincident interfacial nodes are stitched together to create a single unstructured mesh representing the microstructure of the weld. Note that the Voro++ library [18] was used for carrying out the 3D computations of the Voronoi tessellation. A distinguishing feature of this software is that it is able to compute Voronoi diagrams with irregular-shaped domains.

Fig. 4a shows the final developed RVE for a weld fabricated with a welding speed of 3 mm/s and a welding amperage of 120 A. For this set of welding conditions, the results of the welding experiments gave the following input parameters: depth of penetration of 2.8 mm, weld half-width of 3.2 mm and thus at the macro-scale the size of the RVE was 3 mm thick, and 3.5 mm wide (Fig. 4a). At the scale of the microstructure, three regions are clearly visible: base metal with equiaxed grains, columnar zone grains, and equiaxed grains at the center of the weld. Figs. 4b-4d show each of the individual regions. The base metal, Fig. 4b, is composed of polyhedral elements representing equiaxed grains and a fusion surface that follows a parabolic shape obtained from the experimental input data. The columnar zone, Fig. 4c, has elongated polyhedral grains with a length, D , of 330 μm , given by the experimental data. The equiaxed grains at the center of the weld, Fig. 4d, have an average grain size of 60 μm .

Fig. 4e depicts an RVE for a weld fabricated with welding speed of 5 mm/s and amperage of 140 A to demonstrate the ability of the numerical tool to vary the size of the simulation domain and microstructure contained within it as a function of welding parameters. In comparing Fig. 4a and

Fig. 4e, it can be seen that different welding parameters change the size of the weld and also the microstructural features. In this case, the increase in welding speed and amperage has shrunk the weld, and thus the corresponding RVE is reduced in size. Furthermore, the substructure can be easily modified to reflect the effect of grain manipulation techniques that are used to change the microstructure of the weld. Fig. 4f shows the RVE of a weld fabricated with the same welding parameters as of Fig. 4e but with longer columnar zone associated with grain manipulation techniques in which columnar grains are able to grow longer. Physically, this structure could have formed due to a lack of impurities, nucleants or turbulence within the weld pool [16].

After constructing complex 3D Voronoi diagrams such as the one shown in Fig. 4a, each Voronoi cell or grain is subdivided into polyhedral volume elements with the nucleation center as the summit and the Voronoi facet as the base [10]. These pyramids are divided further into tetrahedral elements in order to model solidification. Fig. 5 shows one of the tetrahedral elements. The nucleus of the grain (node 3) forms the apex of the element, and three other vertices (nodes 0, 1, and 2) form the base of a fully-solidified element. The solid/liquid interface is also shown (nodes 4, 5, and 6).

2.2. Thermal analysis

Simulation of solidification during a welding process requires knowledge of the thermal field since solid fraction varies as a function of temperature. The thermal field, T , during welding as a function of spatial coordinates R (radial distance from the center of the weld) and X (distance from the center of the weld along the weld line) can be calculated from the well-known Rosenthal equation,

$$\frac{2\pi(T - T_o)KR}{Q} = \exp\left[\frac{-V(R - X)}{2\alpha}\right] \quad (1)$$

where T_o is the initial temperature of the workpiece, V is the travel speed of the torch, Q is the heat transferred from the torch to the metal, and K and α are the thermal conductivity and diffusivity of the base metal. Although the Rosenthal equation cannot yield precise temperatures above the liquidus, it provides a good prediction of the thermal fields in the mushy zone [16].

In the present model, the temperature evolution at each node of the discretized mesh was calculated from the Rosenthal equation for a given set of welding parameters using a Matlab script. Within an element, the temperature at any position, T^p , was calculated via linear interpolation [19] of the four nodal temperatures, i.e.,

$$T^p = \sum_{i=0}^{i=3} \alpha_i T_i \quad (2)$$

where T_i are the nodal temperatures and α_i are the shape or interpolation functions. At an arbitrary point (p) in the natural coordinate system [19], the values of α_i are given by,

$$\alpha_i |_p = \frac{h_i^p}{h_i} = \frac{V_i^p}{V} \quad (3)$$

$$\sum_{i=0}^{i=3} \alpha_i |_p = 1 \quad (4)$$

where $\alpha_i |_p$ is the value of the i^{th} interpolation function at the point p , h_i^p represents the distance of p to the face opposite to the i^{th} node, h_i is the distance of the i^{th} node to the corresponding face, V is the total tetrahedral volume, and V_i^p represents the volume of the subtetrahedron spanned by the coordinates of the point p and the face opposite the i^{th} node. The definition of these variables is further presented in Fig. 7a and 7b, where $A_i^{s/l}$ represents the relative areas of the solid-liquid interface for each of the shape functions.

2.3. Solidification

The Voronoi tessellation represents the fully solidified microstructure. To model solidification within a tetrahedron, the solid/liquid interface is moved from the nucleus to the base facet, i.e. from node 3 in Fig. 5 towards nodes 0, 1, and 2 with time. At the end of the solidification sequence, tetrahedrons from opposing grains come into contact with each other, and coalesce.

Unlike previous granular-type solidification models [8-10], which used a 1-D microsegregation problem to model the interface evolution, Scheil-type solidification [16, 20, 21, and 22] within individual elements is assumed in this study. This assumption avoids the need for developing a multi-component microsegregation model for the Al-Mg-Si system. In welding, the solidification rates are high and thus the Scheil assumption of complete diffusion in the liquid and no diffusion in the solid is appropriate. The evolution in fraction solid with temperature for AA6061 is plotted in Fig. 6 using a Scheil approximation within the Thermo-Calc software.

The position of the solid/liquid interface within a tetrahedron at a given temperature is given by,

$$x^* = L\sqrt[3]{f_s} \quad (5)$$

where x^* represents the perpendicular distance from the apex of the tetrahedron to the solid/liquid interface, f_s , is the fraction solid at the given temperature as extracted from the Scheil model, and L is the perpendicular length of the element.

In order to apply the curve in Fig. 6 to model granular solidification during welding, a single temperature must be assigned to each element at every time-step of the simulation. Due to the severe thermal gradients in welding, the four nodal temperatures calculated using Eq. (1) could be quite different, and consequently, an average temperature is inappropriate. Instead, it was assumed

that the temperature at the center of the solid/liquid interface, $T_{s/l}$, controls the fraction solid within an element. Note that as the solid/liquid interface is small, the temperature gradient over the interface is negligible and thus, any point on the interface could have been chosen.

Since temperatures within any element are calculated via linear interpolation, the temperature at the center of the solid/liquid interface can be determined using Eq. (2). Based on the node numbering shown in Fig. 5, the value of the third shape function at this location is given by,

$$\alpha_3|_{s/l} = \frac{L - x^*}{L} = 1 - \frac{x^*}{L} \quad (6)$$

Note that the node 3 corresponds to the nucleus of the solidifying element. Due to symmetry, the other three shape functions are equal, as they all have the same base area, $A_0^{s/l} = A_1^{s/l} = A_2^{s/l}$, and the same height from their base to their apex, $H_0^{s/l} = H_1^{s/l} = H_2^{s/l}$. Consequently,

$$\alpha_0|_{s/l} = \alpha_1|_{s/l} = \alpha_2|_{s/l} \quad (7)$$

The combination of Eqs. (5), (6), and (7) give,

$$\alpha_0|_{s/l} = \alpha_1|_{s/l} = \alpha_2|_{s/l} = \frac{X^*}{3L} \quad (8)$$

By substituting Eqs. (6) and (8) into Eq. (3), the temperature at the center of the solid/liquid interface is given by,

$$T_{s/l} = \left(1 - \frac{X^*}{L}\right) T_3 + \left(\frac{X^*}{L}\right) T_{base} \quad (9)$$

where $T_{base} = (T_0 + T_1 + T_2)/3$ corresponds to the arithmetic average of the nodal temperatures at the base of the tetrahedron. Finally, Eqs. (5) and (9) can be combined to yield a master equation controlling the movement of the solid/liquid interface,

$$T_{s/l} = \left(1 - \sqrt[3]{f_{s(T_{s/l})}}\right) T_3 + \left(\sqrt[3]{f_{s(T_{s/l})}}\right) T_{base} \quad (10)$$

where $f_{s(T_{s/l})}$ is the fraction solid in Fig. 6 assuming a temperature at the solid/liquid interface.

The choice of using the solid/liquid interface as the controlling temperature for determining the fraction solid based on Fig. 6, in combination with the fact that there is a strong temperature gradient within an element based on Eq. (2) necessitates that Eq. (10) be solved via an iterative solution. The system equations were thus numerically solved using the Newton-Raphson method for each element to obtain $T_{s/l}$ at each time step. Then, the converged values were applied to Eq. (5) to extract the positions of the interface with time, and therefore, to track the growth of the solid phase within the RVE. Three different images have been inset into Fig. 6 in order to show the evolution of the solid/liquid interface and therefore the simulation of the growth of the solid phase with temperature. In these images, the dark (light) areas represent the liquid (solid) phases.

Since the main purpose of the current model is to simulate at the meso-scale the transient two-phase microstructure of the semisolid weld pool, no attempt has been made to distinguish between primary, eutectic, and secondary phases. All possible products of solidification are treated as a single solid that is evolving with time. In the case of AA6061, this assumption is reasonable since the total amount of eutectic phases is less than 2%. In alloys with increased eutectic content, additional substructure would have to be included within the simulation domain to separate eutectic grains from primary grains so that individual micro liquid channels could become blocked through the sudden growth of a eutectic micro-constituent

2.4. Coalescence

Coalescence during solidification corresponds to the point at which two neighbouring solid grains come into contact with each other and coalesce or bridge [9, 10]. This occurs near the end of solidification; two grains may be in mechanical contact but have not yet fused together, i.e. coalesced, due to thermodynamic considerations. Coalescence plays a large role in defect formation since undercoolings on the order of 75°C below the equilibrium liquidus can be required [8], extending the temperature range where continuous liquid films exist prior to final solidification. The present model utilizes the thermodynamic criterion proposed by Mathier to reflect the nonuniformity of grain coalescence during solidification [13]. Based on this criterion, it is assumed that the neighbour grains with crystallographic misorientations of 15 deg. or less are attractive couples that coalesce immediately as their solidification fronts meet each other. On the other hand, once the misorientations exceed 15 deg., the grains are assumed to be repulsive couples that do not coalesce until a required undercooling is reached. The numerical implementation of this coalescence criterion can be found in Reference [9].

3. Results and discussion

3.1. Structural analysis of the semisolid weld

Fig. 8 shows the type of result that can be obtained under transient welding conditions of 3 mm/s welding speed and 120 A welding amperage, resulting in the microstructure of Fig. 4a. The total number of grains simulated was 4562. As can be seen in Fig. 8, the model is able to reconstruct the evolution in welding microstructure with time. In this figure, the empty space represents the liquid phase, and the filled space represents the individual solid grains.

At a welding time of zero, the RVE is only composed of base metal and a fully liquid weld pool, corresponding to the $t=0$ image in Fig. 1. At this point, all of the elements within the weld pool

are assumed to be in the liquid state. As the welding torch advance, the RVE cools, enabling solidification. The temperature of the columnar elements close to the fusion surface falls below the liquidus temperature, and as shown in Fig. 8a (0.2 s after start of welding), the solidifying columnar grains start to grow towards the weld centerline. The elements within the solidifying grains are each composed of both liquid and solid, separated through the solid/liquid interface, though only material that is solid can be seen. At each time-step, the nodal temperatures are calculated using the Rosenthal equation, and the location of the solid/liquid interface is determined assuming Scheil conditions for solidification. As time progresses, the equiaxed grains at the center of the weld will gradually start to form, and eventually block the growth of the columnar zone, i.e. the Columnar-to-Equiaxed transition. Note, however, that the model does not specifically simulate the CET since the length of the columnar zone is fixed as a model input based on the experimental data shown in Figs 2 and 3. The state at which the centerline equiaxed grains first nucleate and block the advancing columnar grains is shown in Fig. 8b, 0.7 s after start of welding. Fig. 8c, 1.8 s after start of welding, represents the microstructure at a later time once the welding torch moves further away from the RVE. The given images also show the formation of micro liquid channels within the mushy zone. These channels are located along the grain boundaries, and form a continuous network of liquid linking the base of the columnar grains with the center of the weld pool. As solidification proceeds, smaller channels will close while larger ones remain open. As can be seen, the micro liquid channels become narrower with the transition from Fig. 8a to Fig. 8c; at later stages they will finally become blocked due to coalescence.

The ability of the present model to create a mushy zone structure at the meso-scale composed of many solidifying grains and an interlocking network of micro liquid channels is an important step towards modelling solidification defects [3, 23, and 24]. In comparison, existing solidification

models for welding are not able to provide a proper replica of the structure of the semisolid weld upon which to perform fluid-flow and deformation simulations [9, 10] for predicting hot crack formation. The majority of the previous models (e.g. [4-6]) focus on only a few grains, and thus, cannot simulate the network of micro liquid channels. Although some of the models extend their simulation domain over a larger number of grains (e.g. [7, 25]), they still suffer from ignorance of the third dimension. Sistaninia *et al.* [10] has shown that consideration of 3D effects is key for predicting hot crack formation since it strongly affects the continuity of the micro liquid channel network. In the future, the current model will be expanded to investigate transient phenomena within the semisolid weld such as cavitation, the formation of micro-cracks, and also flow characteristics.

3.2. Case Study: Effect of welding procedure on semisolid weld characteristics

The new meso-scale welding model can be used to investigate the effects of welding procedure on semisolid weld characteristics. A key microstructural feature affecting the feeding ability of the mushy zone is the width of the micro liquid channels [3, 10]; the wider the channels are, the easier they can feed the molten metal into to the solidifying weld pool and hence reduce hot cracking. In a dendritic microstructure, like welding, micro liquid channels within a semisolid medium can be classified into two major types: 1) interdendritic channels that circulate the molten metal through the interdendritic spaces within the solidification envelope of a single grain, and 2) intergranular channels forming between neighbouring grains. The role of the intergranular channels is to feed molten metal into the interdendritic regions to counteract solidification shrinkage. The current simulation does not include dendritic features of the grains, and thus only the meso-scale feeding ability, given by the width of the intergranular micro liquid channels, can be analyzed. A future

study that includes fluid-flow will take into account both the intergranular and interdendritic channels.

As shown in Fig. 2, the choice of welding speed and welding power directly affects grain morphology. The flexibility of the new meso-scale welding model enables study of these effects in order to link variability in the width of the micro liquid channels processing. Figs. 9 to 11 present an analysis showing the effects of grain manipulation techniques and welding parameters on the average width and standard deviation of micro liquid channels. As the critical solid fraction in which the feeding ability of the weld pool will directly influence hot cracking is known to occur between $0.8 < f_s < 0.9$ [16, 26], the analysis was carried out only on micro liquid channels located between grains in this range. Good feeding is assumed to occur at values less than $f_s = 0.8$, while little or no feeding is assumed to occur for $f_s > 0.9$. Moreover, since the microstructure of the weld pool is composed of both columnar and equiaxed grains, the micro liquid channels were classified into three different groups based on location: amongst the columnar grains, between columnar and equiaxed grains, and finally amongst the equiaxed grains at the center of the weld. Note that both the average width of micro liquid channels for each group, and the corresponding error with a confidence interval of 68% are reported.

The effect of grain manipulation techniques such as addition of nucleants to the weld pool on micro liquid channels is shown in Fig. 9 (equiaxed grain size) and Fig. 10 (length of columnar grains). The simulation assumed a welding speed of 5 mm/s and amperage of 140 A. As can be seen in both figures, the weld mushy zone does not have a uniform network of micro liquid channels, and therefore different areas of the weld show a non-uniform feeding ability. This is due to the use of a Voronoi tessellation of the solidification nuclei that also causes nonuniformity in grain size.

It should also be noted that the model defines the half-width of a micro liquid channel (W_c) as outlined below based:

$$W_c = L - X^* = L(1 - \sqrt[3]{f_s(T_{s/l})}) \quad (11)$$

As indicated by this form of Eq. (5), at a given solid fraction, the length of an element, L , is the only term that affects the width of the liquid channels. In other words, a dense arrangement of nuclei generates smaller elements and consequently causes channels to shrink, whereas a sparse arrangement of nuclei creates wider channels at the same solid fraction.

Fig. 9 shows that lowering of the density of equiaxed nuclei, and thus, enlarging the equiaxed grains at the center of the weld widens the micro liquid channels both amongst the equiaxed grains and also between the columnar and equiaxed regions. In this case, since the arrangement of the columnar nuclei remains unchanged, the width of these channels does not vary. Fig. 10 shows that the length of the columnar grains also has little effect on either the micro liquid channels within the columnar zone or within the equiaxed zone. Together, however, Figs. 9 and 10 reveal that the micro liquid channels between the columnar and equiaxed grains are always the widest, and that the micro liquid channels amongst the columnar grains usually have the smallest width. This observation can be explained through the fact that the columnar grains are normally quite long, and therefore there is a severe lack of nuclei through the area between the columnar and equiaxed nuclei. On the other hand, the dense arrangement of the columnar nuclei shrinks the channels among the columnar grains as compared to the equiaxed grains.

The influence of welding parameters on the micro liquid channels is shown in Fig. 11. The results for eight different case studies, listed in Table 1, are given. In these cases, the welding speed was varied from 2 to 5 mm/s while the amperage was varied from 110 – 140 A. The results indicate

that welding parameters strongly affect the width of the liquid channels in different areas of the mushy zone and consequently affect the feeding ability of the solidifying weld pool. These observations are due to the fact that various welding parameters change the microstructure and consequently the arrangement of the solidification nuclei within the weld. For instance, the narrow micro liquid channels between the columnar grains and the equiaxed grains for a weld fabricated by welding speed of 4 mm/s and amperage of 130 A can be associated with the short columnar grains in this weld (Fig. 3).

Since the structural characteristics of a semisolid medium affect the deformation behaviour [10] and feeding ability [9] of the semisolid, and consequently formation of hot cracks [27], the obtained results of this model suggest that welding procedure directly influences the formation of hot cracks within the weld pool. Hence, modification of welding procedure can be assumed as a potential technique to prevent hot cracking in welding.

3.3. Model limitations

As shown in the figures above, the model is able to simulate microstructure transitions during solidification within the weld pool, and is quite sensitive to processing parameters. However, a few limitations should be mentioned. First, this modelling approach does not consider the dendritic morphology of grains but instead assumes that the solidification envelope defines the solid-liquid boundary. As discussed in section 3.2, this assumption restricts the capability of the model to assessing only the meso-scale feeding ability of the mushy zone through analysis of the width of the intergranular micro liquid channels, while ignoring the interdendritic micro liquid channels. Second, despite the fact that the growth angle of the columnar grains in the weld microstructure varies with welding parameters [16], the model assumes that the columnar grains always grow

normal to the fusion surface. Third, the columnar-to-equiaxed transition does not occur naturally within the model but instead is imposed by the placement of the grain nuclei.

4. Conclusion

A 3D meso-scale model simulating fusion welding of aluminum – magnesium – silicon alloys has been developed that directly models the evolving semisolid microstructure composed of micro liquid channels and solidifying grains on a relatively large domain. By coupling modified Voronoi diagrams with experimental data, the simulation precisely predicts the shape and size of the weld pool. The results demonstrate that mushy zone features strongly depend on welding parameters, and quantifies the effects of welding procedure on both the macrostructure and also the evolving solidification microstructure. The model indicates that the ability of the mushy zone to feed molten metal into the solidifying areas is not uniform throughout the weld as the micro liquid channels between the columnar zone and equiaxed fusion zone provide the best feeding. This modelling framework is thus a first step towards simulating hot cracking during fusion welding based on the combined behaviour of individual grains and welding parameters.

Acknowledgments

The authors wish to thank the American Welding Society (AWS) and the Natural Sciences and Engineering Research Council of Canada (NSERC) for financial support.

References

- [1] Dye D, Hunziker O, Reed, RC. Acta Mater 2001; 49:683-697.
- [2] Boettinger WJ, Coriell SR, Greer AL, Karma A, Kurz W, Rappaz M, Trivedi, R. Acta Mater 2000; 48:43-70.

- [3] Vernède S, Jarry P, Rappaz, M. Acta Mater 2006; 54: 4023-4034.
- [4] Fallah V, Amoorezaei M, Provatas N, Corbin SF, Khajepour, A. Acta Mater 2012; 60:1633-1646.
- [5] Montiel D, Liu L, Xiao L, Zhou Y, Provatas, N. Acta Mater 2012; 60:5925-5932.
- [6] Zhong XH, Dong ZB, Wei YH, Ma, R. J Cryst Growth 2009; 311:4778-4783.
- [7] Bordreuil C, Niel, A. Comp Mater Sci 2014; 82:442-450.
- [8] Vernède S, Rappaz, M. Acta Mater 2007; 55: 1703-1710.
- [9] Sistaninia M, Phillion AB, Drezet JM, Rappaz, M. Acta Mater 2012; 60: 3902-3911.
- [10] Sistaninia M, Phillion AB, Drezet JM, Rappaz, M. Acta Mater 2012; 60: 6793-6803.
- [11] Vernède S, Rappaz, M. Philos Mag 2006; 86: 3779-3794.
- [12] Phillion AB, Vernède S, Rappaz M, Cockcroft SL, Lee, PD. Int J Cast Met Res 2009; 22: 240-243.
- [13] Mathier V, Jacot A, Rappaz, M. Modelling Simul mater Sci Eng 2004; 12: 479-490.
- [14] Phillion AB, Cockcroft SL, Lee, PD. Acta Mater 2008; 56: 4328-4338.
- [15] Zaragoci JF, Silva I, Bellet M, Gandin CA. IOP C Ser Mater Sci Eng 2012; 33:012054.
- [16] Kou S. Welding Metallurgy, Second ed. New Jersey: John Wiley & Sons; 2003.
- [17] Bonifaz EA, Richards, NL. Acta Mater 2009; 57: 1785-1794.
- [18] <http://math.lbl.gov/voro++/doc/>

- [19] Brenner SC, Scott LR. The Mathematical Theory of Finite Element Methods. New York: Springer-Verlag; 1994.
- [20] Yan X, Chen S, Xie F, Chang YA. Acta Mater 2002; 50: 2199-2207.
- [21] Wang H, Liu F, Yang G, Zhou Y. Acta Mater 2010; 58: 5411-5419.
- [22] Clyne TW, Kurtz, W. Metall Trans A 1981, 12A: 965-971.
- [23] Sistaninia M, Terzi S, Phillion AB, Drezet JM, Rappaz, M. Acta Mater 2013; 61: 3831-3841.
- [24] Vernède S, Dantzig JA, Rappaz, M. Acta Mater 2009; 57: 1554-1569.
- [25] Niel A, Bordreuil C, Deschaux-Beaume F, Fras, G. Sci Technol Weld Joi 2013; 18: 154-160.
- [26] Coniglio N, Cross, CE. Int Mater Rev 2013, 58:375-397.
- [27] Rappaz M, Drezet JM, Gremaud, M. Metall Mater Trans A 1999; 30A: 449-455.

Figure captions

Fig. 1. The base geometry and relative position of the RVE at various welding time.

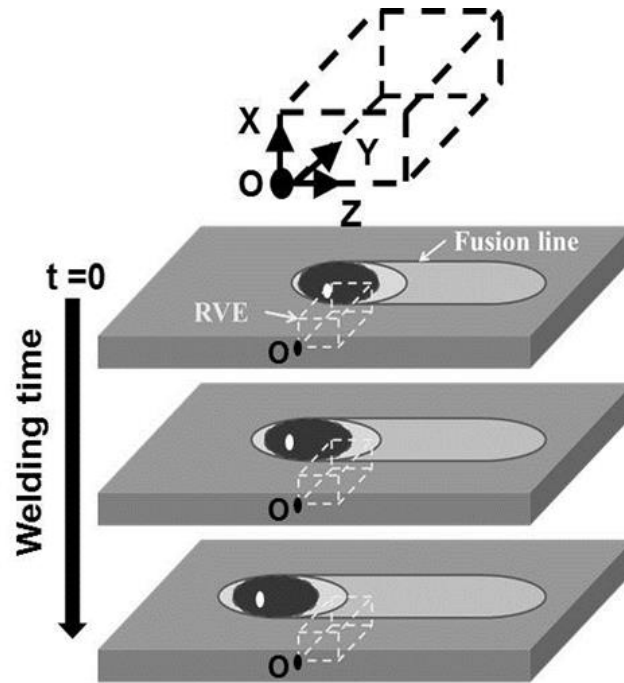


Fig. 2. Example scanning electron microscopy images showing the measurement methodology for (a) depth of penetration, and (b) weld width.

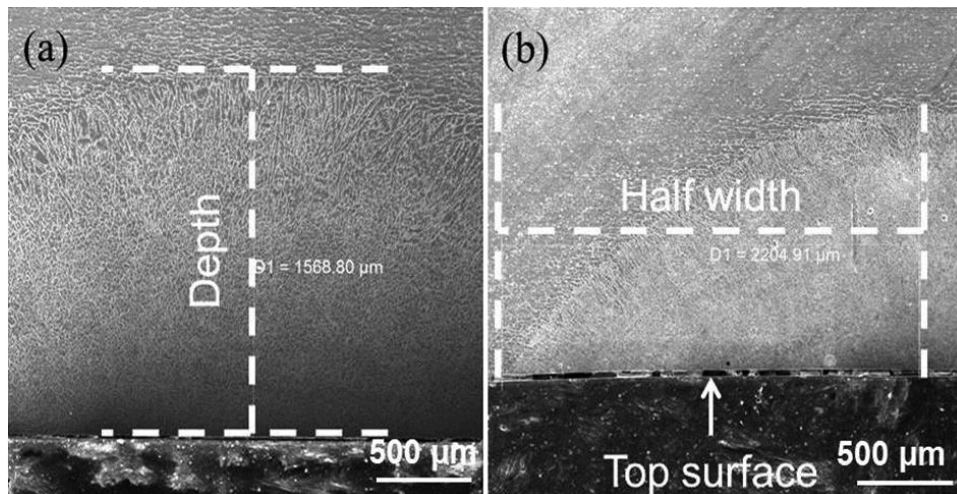


Fig. 3. Process maps from welding experiments linking weld characteristics to welding parameters including amperage and speed: (a) Depth of penetration, (b) Weld half-width, and (c) Normalized length of the columnar zone.

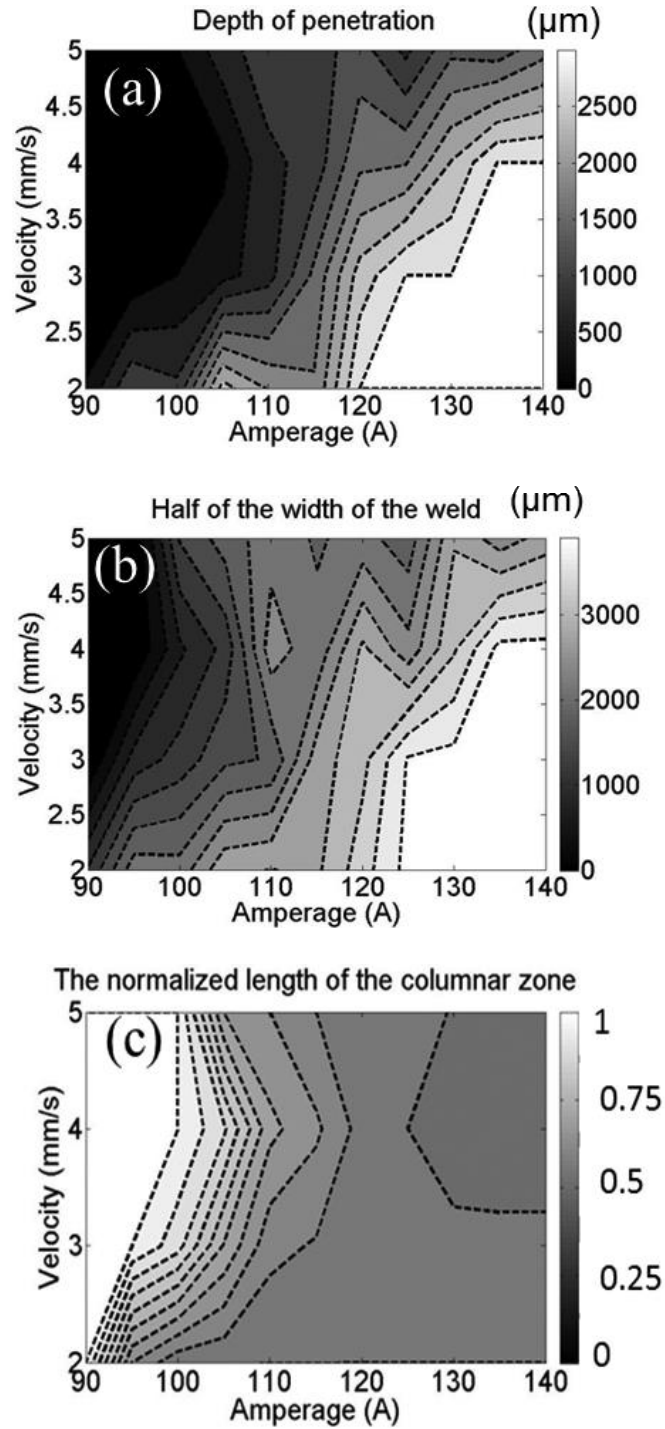


Fig. 4. (a) Developed geometry of the weld mushy zone for a welding speed of 3 mm/s and welding amperage of 120 A; (b) base metal grains; (c) columnar grains; (d) equiaxed grains at the center of the weld; (e) geometry of weld mushy zone fabricated with difference conditions (welding speed of 5 mm/s, welding amperage of 140 A); (f) the same mushy zone as (e) but with longer columnar grains.

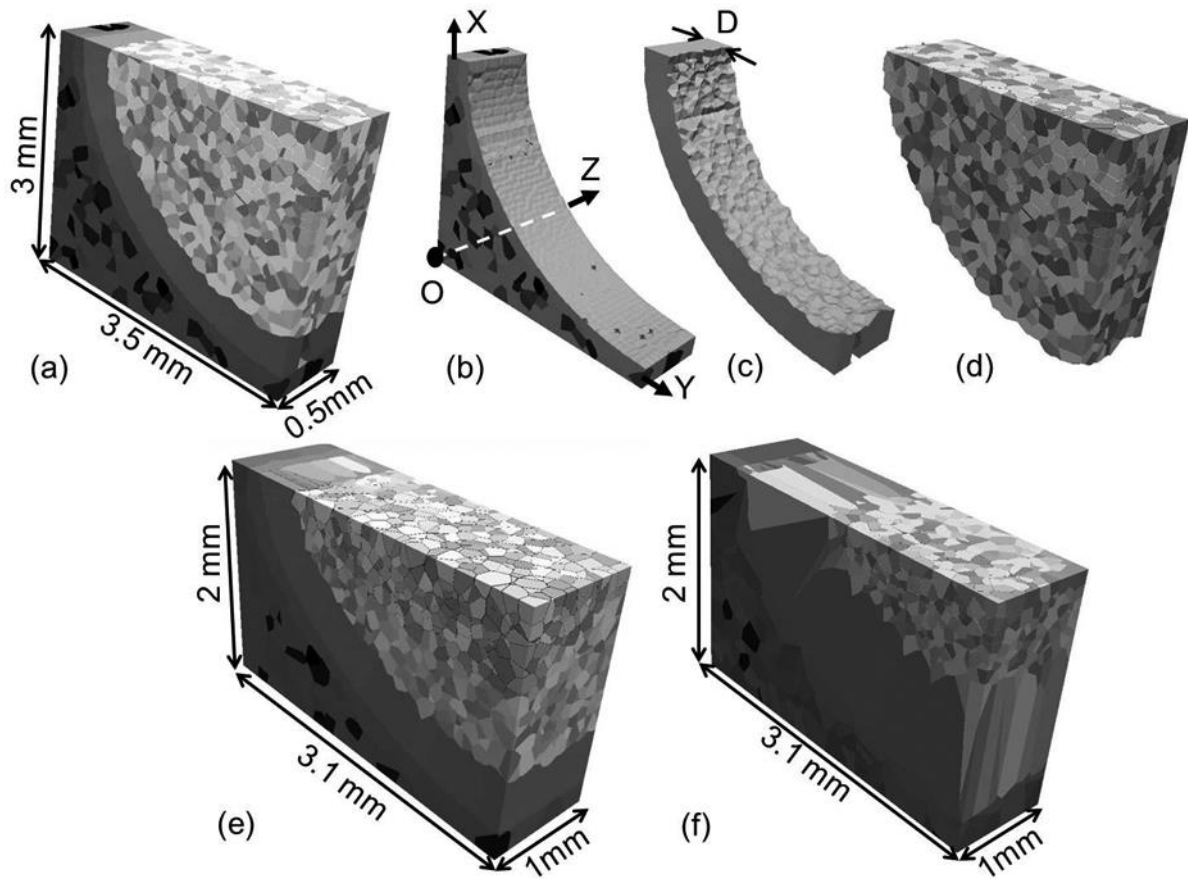


Fig. 5. Schematic of a primary tetrahedral element.

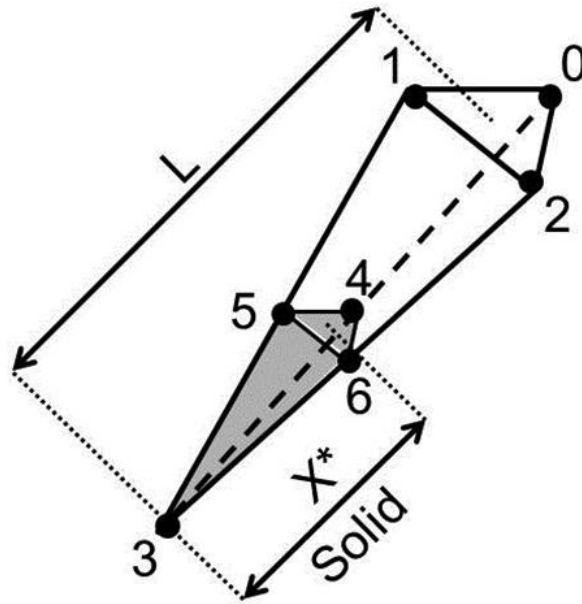


Fig. 6. The relation between the solid fraction and temperature for aluminum 6061 using a Scheil approximation within the Thermo-Calc software. Points 1, 2, and 3 and their corresponding images show the growth of the solid phase within the model during cooling.

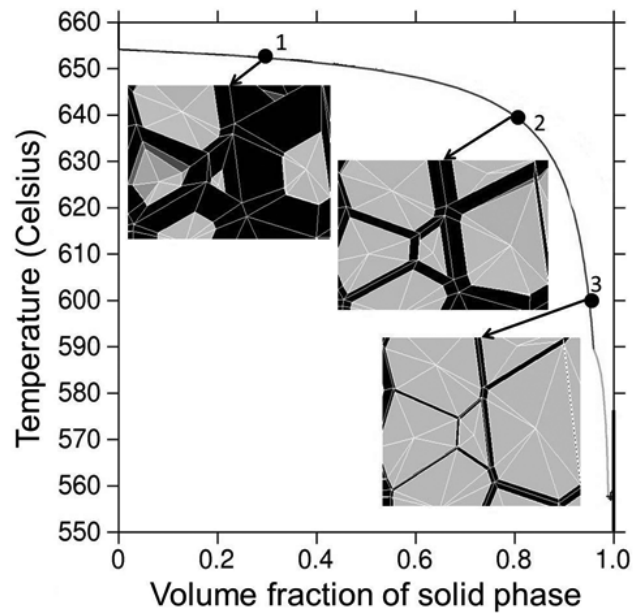


Fig. 7. (a) A reference tetrahedron element showing an arbitrary point (p), the face opposite the i^{th} node, subtetrahedron volume (V_i^p) spanned by the point p and the i^{th} face, and also the distance of the point from the i^{th} face (h_i^p). (b) Shows the center of the triangular solidification front, and the geometrical characteristics (the area of the base (A_i^p), and the height from the apex to the base (H_i^p)) of the subtetrahedrons spanned by the coordinates of the centroid and the faces opposite the nodes 0,1, and 2.

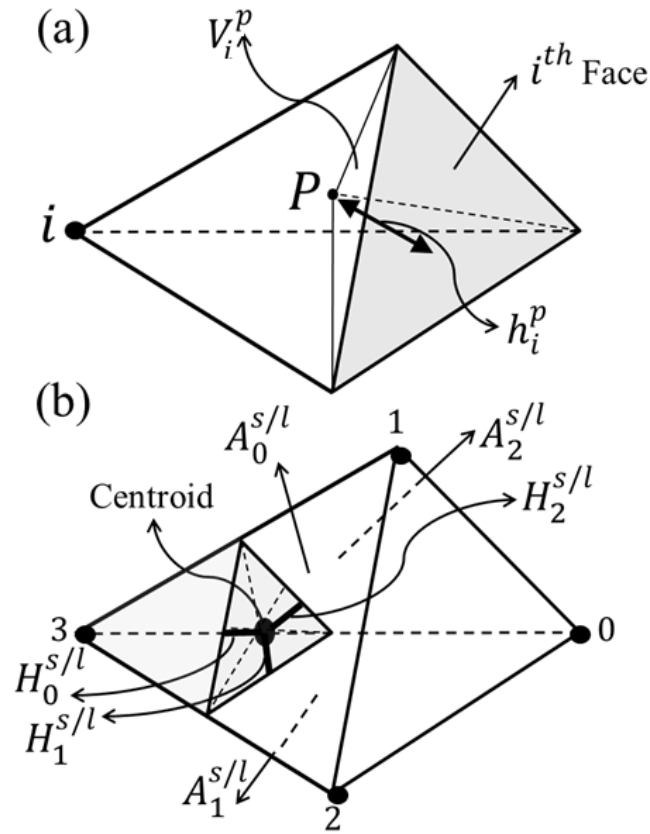


Fig. 8. The gradual evolution of the weld mushy zone as predicted by the model at welding time of (a) 0.2 s, (b) 0.7 s, and (c) 1.8 s. The weld was fabricated using a welding speed of 3mm/s and welding amperage of 120 A.

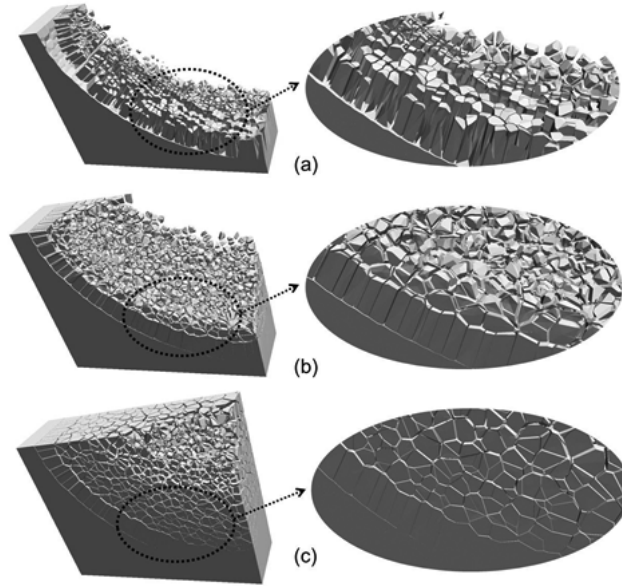


Fig. 9. Process map from a series of simulations examining the effect of equiaxed grain size at the center of the weld on the average width of the micro liquid channels near grains with high f_s .

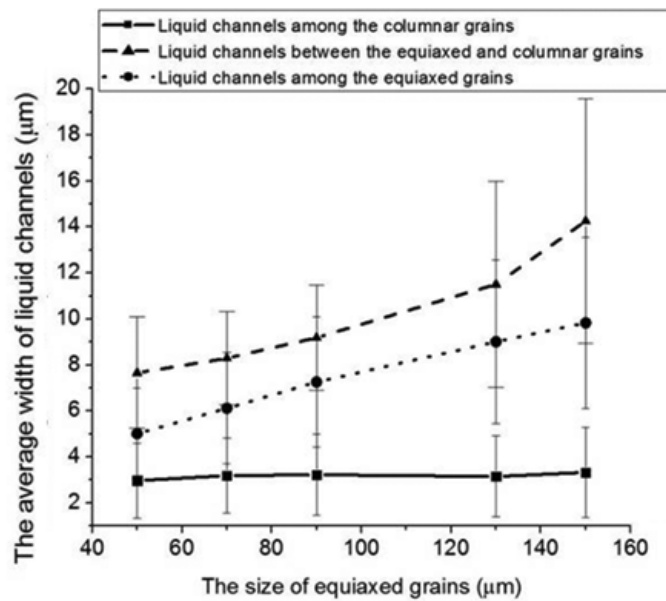


Fig. 10. Process map from a series of simulations examining the effect of columnar grain length on the average width of the micro liquid channels near grains with high f_s .

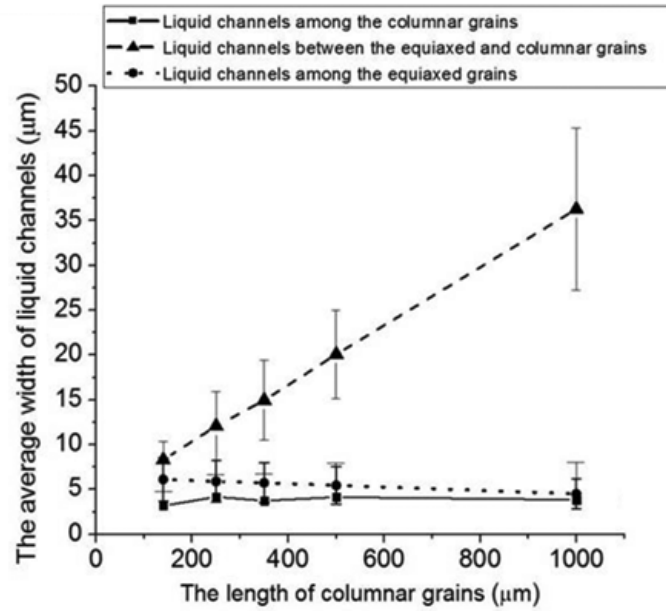


Fig. 11. Process map from a series of simulations examining the effect of welding parameters on the average width of the micro liquid channels near grains with high f_s .

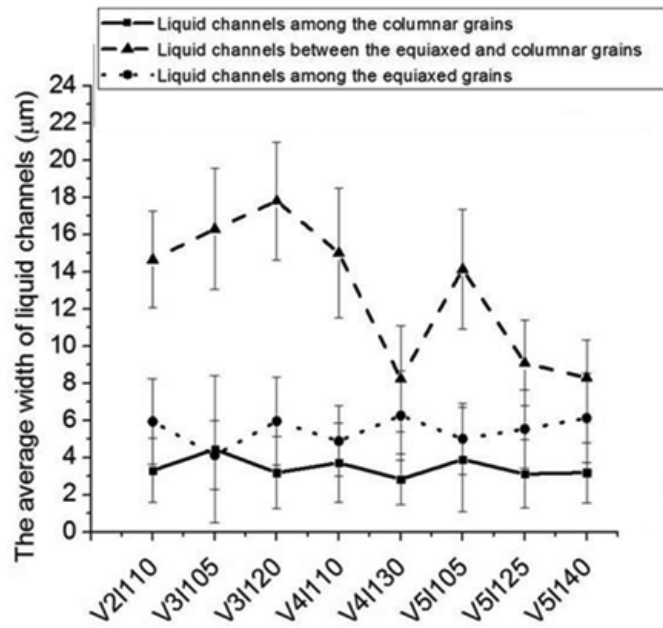


Table captions

Table 1. Welding parameters and resulting microstructure for the simulations examined in Fig. 11.

Case study	Welding speed (mm/s)	Welding amperage (A)	The size of the base metal grains (μm)	The size of the columnar grains (μm)	The size of the equiaxed grains (μm)	Depth of penetration (μm)	The width of the weld (μm)
V2I110	2	110	80	220	65	2300	3300
V3I105	3	105	80	220	55	800	2000
V3I120	3	120	80	330	60	2800	3500
V4I110	4	110	80	350	48	1100	2800
V4I130	4	130	80	130	65	2700	3500
V5I105	5	105	80	310	55	1000	2200
V5I125	5	125	80	130	65	1100	2200
V5I140	5	140	80	140	68	2000	3100